

denoiSplit: a method for joint image splitting and unsupervised denoising

Ashesh¹ and Florian Jug¹

Fondazione Human Technopole, Viale Rita Levi-Montalcini 1, 20157 Milan, Italy
ashesh276@gmail.com; florian.jug@fht.org

Abstract. In this work we present denoiSplit, a method to tackle a new analysis task, *i.e.* the challenge of joint semantic image splitting and unsupervised denoising. This dual approach has important applications in fluorescence microscopy, where semantic image splitting has important applications but noise does generally hinder the downstream analysis of image content. Image splitting involves dissecting an image into its distinguishable semantic structures. We show that the current state-of-the-art method for this task struggles in the presence of image noise, inadvertently also distributing the noise across the predicted outputs. The method we present here can deal with image noise by integrating an unsupervised denoising sub-task. This integration results in improved semantic image unmixing, even in the presence of notable and realistic levels of imaging noise. A key innovation in denoiSplit is the use of specifically formulated noise models and the suitable adjustment of KL-divergence loss for the high-dimensional hierarchical latent space we are training. We showcase the performance of denoiSplit across 4 tasks on real-world microscopy images. Additionally, we perform qualitative and quantitative evaluations and compare results to existing benchmarks, demonstrating the effectiveness of using denoiSplit: a single Variational Splitting Encoder-Decoder (VSE) Network using two suitable noise models to jointly perform semantic splitting and denoising.

1 Introduction

Fluorescence microscopy remains a cornerstone in the exploration of cellular and sub-cellular structures, enabling scientists to visualize biological processes at a remarkable level of detail [9, 23]. The ability to distinguish and analyze multiple structures within a single sample, though, requires a multiplexed imaging protocol that requires extra time and effort [23]. To address these downsides, and enable more efficient and new kinds of investigations, a powerful method for semantic image splitting was recently introduced [1].

Building upon this previous work [1], we address a key challenge that persisted: noise in microscopy images and its adverse effect on the quality of image splitting predictions. Recognizing the need for a method capable of handling noisy input images while maintaining the integrity of the semantic splitting task, we introduce a technique that not only builds on the strengths of

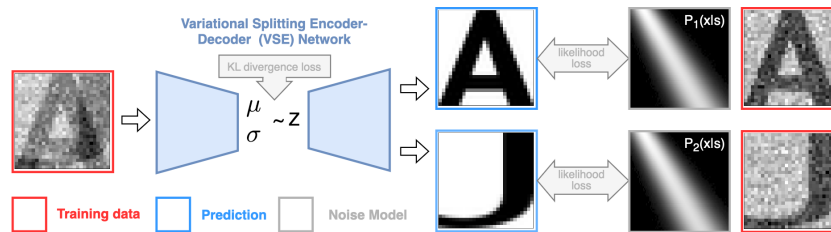


Fig. 1: Teaser Figure. In this work we use a variational encoder-decoder network to jointly solve an unsupervised denoising and image splitting task and show that our approach outperforms sensibly chosen baselines.

μ Split [1] but also incorporates unsupervised denoising capabilities, for example as in [16, 20–22]. Figure 1 outlines the overall approach we are proposing.

Combined, these ingredients lead to a new method, denoiSplit. It refines the process of image decomposition, ensuring that even under high levels of pixel noises present in the entire body of available training data, the semantic integrity of the semantically split image components (the predictions) is well preserved. Additionally, denoiSplit can assess data uncertainty by sampling from the learned posterior of possible splitting solutions, followed by evaluating the inter-sample variability. Additionally, in Section 4, we show how to use this possibility to predict the expected error denoiSplit makes on a given input. In supplementary Sec S3, we pen down a concrete pipeline which microscopists can follow to assess the possibility of using our work without making any change to their microscope configuration.

In summary, we believe that this work will open new avenues for the efficient and detailed analysis of complex biological samples, for example in the context of fluorescent microscopy.

2 Related Work

2.1 Image Denoising

Image denoising is a task that has a long and exciting history. Classical methods, such as Non-Local Means [5] or BM3D [6], were frequently and very successfully used before neural network based approaches have been introduced towards the end of the last decade [15, 26–28].

The advent of deep learning saw people exploit different aspects of noise and the way networks learn to enable denoising. Noise, while usually being undesired, is simultaneously much harder to predict, as was elegantly demonstrated in [25], leading to a zero-shot denoiser. In the case specific to pixel noises, *i.e.* all forms of noise that are independent per image pixel (given the signal at that pixel) [23], the impossibility to predict the noise was exploited in various ways, leading to important contributions such as Noise2Void [15], Noise2Self [3], or Self2Self [14]. Another well known approach close to this family of approaches

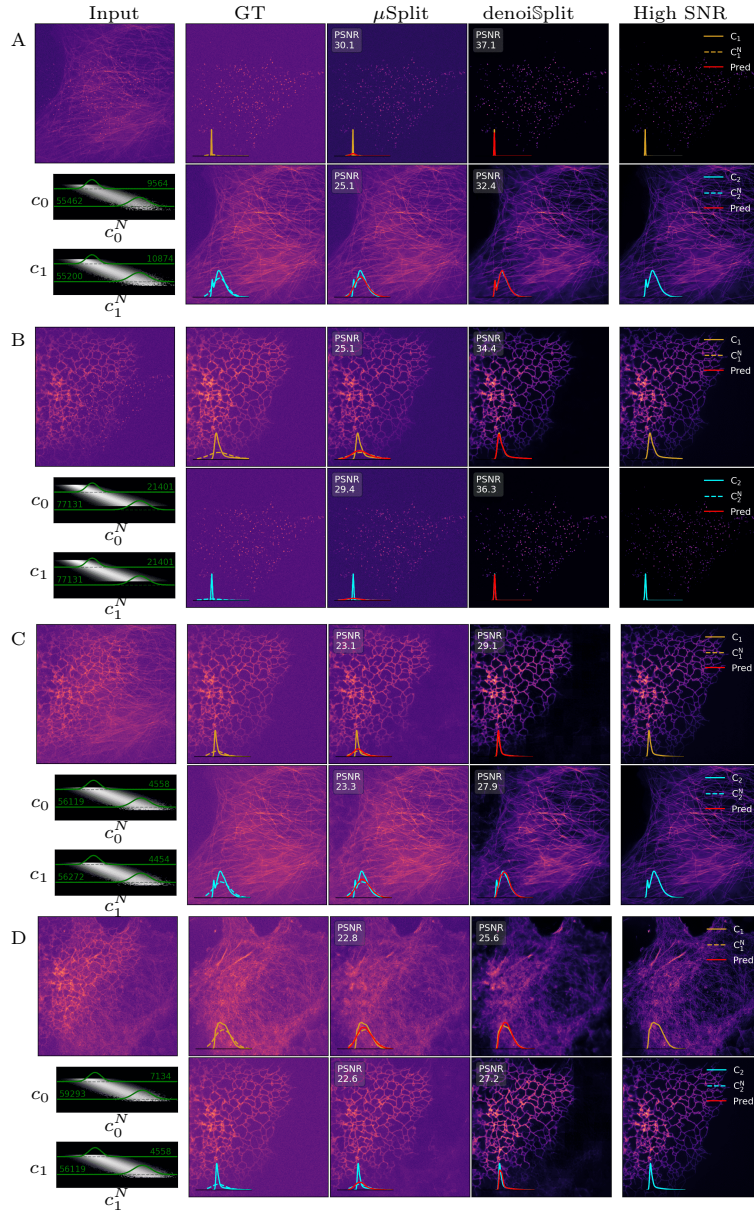


Fig. 2: Qualitative Results. We show examples of noisy inputs, individual noisy channel training data (GT), and predictions by one of the baselines (μ Split) and our own results obtained with denoiSplit for all four tasks (A: MT vs. CCPs, B: ER vs. CCPs, C: MT vs. ER, and D: F-actin vs. ER). Additionally we show high SNR channel images (not used during training) and show PSNR values w.r.t. these images. Additionally, we plot histograms of various panels for comparison (see legend on the right). The bottom cell in the first column of each panel shows the used noise models (see main text for details). The superimposed plots (green) show the distribution of noisy observations (c_i^N) for two clean signal intensities.

is Noise2Noise [17], capable of denoising even more complex noises that can correlate beyond the confines of single pixels.

Slightly later, to further improve denoising performance, Probabilistic Noise2Void [16, 22] introduced, and DivNoising [21] and Hierarchical DivNoising (HDN) [20] reused the idea of suitably measured or trained pixel noise models. Such noise models are, in essence, a collection of probability distributions mapping from a true pixel intensity to observed noisy pixel measurements (and vice-versa).

2.2 Image Decomposition

Image decomposition is the inverse problem of splitting a given input image that is the superposition (*i.e.* the pixel-wise sum) of two constituent image channels. While the sum of two values is not uniquely invertible, if for each summand a prior on its value exists, a unique solution can exist. In a similar vein, having learned structural priors of the appearance of the two constituent image channels, an input image (a grid of observed pixels that are each a sum of two values) can be split into two pixel grids such that each one satisfies the respective structural prior. In computer vision, reflection removal, dehazing, deraining *etc.* are some of the applications [2, 4, 7, 8] for which image splitting can be used.

More recently, image splitting in fluorescence microscopy was experiencing heightened attention, likely due to the direct applicability and potential utility a well working approach can bring to this microscopy modality that finds widespread use in biological investigations. In particular, a method called μ Split [1] demonstrated impressive image splitting performance on several datasets, suggesting that it is ready to be used in biological research projects.

However, μ Split's requires relatively noise-free data for training and prediction, which limits its potential utility (see also Section 5 or Figure 2).

2.3 Uncertainty Calibration

The ability to correctly assess the quality of predictions is of obvious utility. Ideally, a predictive system capable of co-predicting a confidence value, has the property that the predicted confidence scales with the average error of the prediction. If the relationship between error and confidence is close to the identity, we call the uncertainty predictions of this system *calibrated*.

Early works tried to use the deviation of the prediction as a proxy for the confidence in the made predictions [27]. Other works tried to calibrate the predicted standard deviation with the expected error (*i.e.* the RMSE) [18]. Earlier calibration works were mostly concerned with classification tasks [19]. However, in [18], those approaches were reformulated in the context of regression.

In [18], the authors propose a way to evaluate calibration. They train a separate branch to predict a standard deviation per pixel that expresses its prediction uncertainty. For evaluating the calibration quality, the authors cluster examples on the basis of the predicted standard deviation values. Within each cluster, the

predicted uncertainty is then compared with the empirical uncertainty (RMSE loss). To further improve the calibration, the authors propose a simple, yet effective scaling methodology wherein they learn a scalar parameter on re-calibration data, *i.e.* a subset of data not included in the training data. (In our experiments, we use the validation data for this purpose.) This scalar gets multiplied to the predicted uncertainty values, which then reduces the calibration error.

3 Problem Formulation

Lets denote a noise free dataset containing n pairs of images as $D = (C_1, C_2)$, with each C_i containing n two-channel images $C_i = (c_{i,j} | 1 \leq j \leq n)$. Lets define a corresponding set of images $X = (x_j | 1 \leq j \leq n)$, such that all $x_j = c_{1,j} + c_{2,j}$ are the pixel-wise sum of the two corresponding channel images.

While D is typically not available (or even observable), in practice we can only observe noisy data, denoted here by $D^N = (C_1^N, C_2^N)$. Analogous to before, we define $X^N = (x_j^N | 1 \leq j \leq n)$, such that $x_j^N = c_{1,j}^N + c_{2,j}^N$ are the pixel-wise sum of the noisy channel observations.

Given one $x_j^N \in X^N$ of D^N , the task at hand is to predict the noise free and unmixed tuple $(c_{1,j}, c_{2,j})$. We shall denote the predictions made by a trained denoiSplit network by $(\hat{c}_{1,j}, \hat{c}_{2,j})$.

Whenever above notions are used in a context that makes the j in the subscript redundant, we allow ourselves to omit them for brevity and readability.

For evaluation purposes, we will in later sections use high-quality microscopy datasets that contain minimal levels of noise as surrogates for D , X , C_1 , and C_2 , but we never use them during training, and only their noisy counterparts are used.

4 Our Approach

In the following sections we describe the main ingredients of denoiSplit, namely the hierarchical network structure we use (Section 4.1), the changed loss term for variational training of the splitting task (Section 4.2), the noise models we employ to enable the joint unsupervised denoising (Section 4.3), and an uncertainty calibration methodology allowing us to estimate the prediction error introduced by aleatoric uncertainty in a given input image (Section 4.4).

4.1 Network Architecture and Training Objective

In this work, we employ an altered Hierarchical VAE (HVAE) network architecture. HVAEs were originally described in [24] and later adapted for image denoising in [20] and for image splitting in [1]. In general terms, HVAEs learn a hierarchical latent space, with the lowest hierarchy level encoding detailed pixel-level structure, while higher hierarchy levels capture increasingly larger scale structures in the training data.

For denoiSplit, we modify the HVAE architecture to not any longer being used as an autoencoder. Instead, our outputs are the two unmixed channel images (\hat{c}_1, \hat{c}_2) , motivating us to call the resulting architecture a Variational Splitting Encoder-Decoder (VSE) Network.

Our objective is to maximize the likelihood over the noisy two channel dataset we train on, *i.e.*, finding decoder parameters θ such that

$$\theta = \arg \max_{\theta} \sum_{1 \leq j \leq n} \log P(c_{1,j}^N, c_{2,j}^N; \theta). \quad (1)$$

Using the modified evidence lower bound (ELBO), as proposed in [1] and assuming conditional independence of the two predictions given the latent space embedding, we maximize

$$E_{q(z|x; \phi)} [\log P(c_1|z; \theta) + \log P(c_2|z; \theta)] - KL(q(z|x; \phi), P(z)), \quad (2)$$

where $q(z|x; \phi)$ is the distribution parameterized by the encoder network output $\text{Enc}_{\phi}(x)$, $P(c_1|z; \phi)$ is the distribution parameterized by decoder network output $\text{Dec}_{\theta}(z)$ and $KL()$ denotes the Kullback-Leibler divergence loss. As in [1], $P(z)$ factorizes over the different hierarchy levels in the network. Please refer to [1] for a more thorough derivation. Details about the training, hyperparameters used, and used VSE Networks can be found in the supplementary Sec S2.

Similar to the way noise models had been employed in the context of denoising [20], we model the two log likelihood terms $\log P(c_1|z; \theta)$ and $\log P(c_2|z; \theta)$ using noise models which we describe in detail in Section 4.3 and naturally in our open code repository.

4.2 Hierarchical KL Loss Weighing for Variational Training

In μSplit , the authors showed SOTA performance on a multitude of splitting tasks. However, used datasets were close to noise-free, making the task at hand simpler than the one we outlined in Section 3. When μSplit is trained on noisy datasets, the resulting channel predictions are themselves noisy. After analyzing this matter, we concluded that a modified KL loss can help to reduce the amount of noise being reconstructed by the decoder.

In more technical terms, let Z be a hierarchical latent space and $Z[i]$ denote the latent space embedding at i -th hierarchy level, having shape (c, h_i, w_i) , with c being channel dimension, and h_i, w_i the height and width of the latent space embedding. Now let KL_i denote the KL-divergence loss tensor computed on $Z[i]$, which has the same shape as $Z[i]$ itself.

In μSplit , the corresponding scalar loss term kl_i is defined as

$$kl_i = \alpha \cdot \sum_{j,h,w} \frac{KL_i[j, h, w]}{h_i \cdot w_i}, \quad (3)$$

with α being a suitable constant. Observe that the denominator makes each kl_i be the average of all values in KL_i , making the respective values not scale with

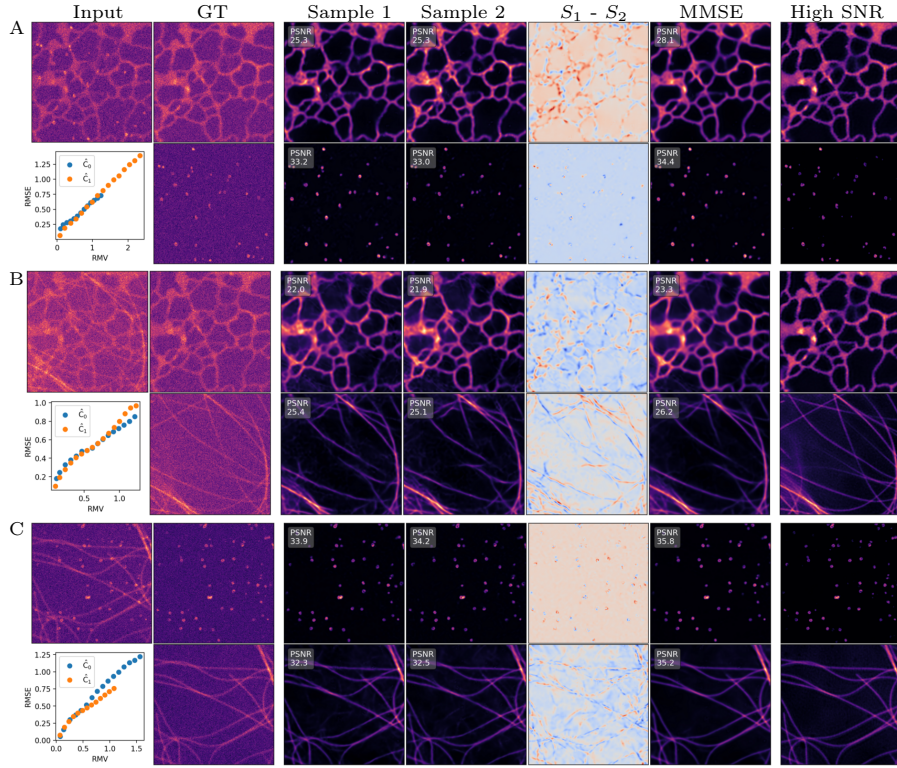


Fig. 3: Variational Sampling and Calibration. The VSE Network in denoiSplit is capable of sampling from a learned posterior. Here we show cropped inputs (256×256), two corresponding prediction samples, the difference between the two samples ($S_1 - S_2$), the MMSE prediction, and otherwise unused high SNR microscopy for three tasks, namely ER vs. CCPs, ER vs. MT, and CCPs vs. MT. The MMSE predictions are computed by averaging 50 samples. As before, we show PSNR w.r.t. high SNR patches. The dot plots in the first column show are calibration plots, showcasing that the error estimate we propose works well (see main text).

the size of $Z[i]$, even though lower hierarchy levels ($Z[i]$ for smaller i) have more entries. However, this also means that the KL loss for the individual pixels in these lower hierarchy levels is given less weight. Hence, smaller structures, such as noise itself, can more easily seep through such pixel-near hierarchy levels.

In this work, we diverge from this formulation and return to a more classical setup where we compute the scalar loss term for the i -th hierarchy level $Z[i]$ as

$$\text{kl}_i = \alpha \cdot \sum_{j,h,w} \text{KL}_i[j, h, w]. \quad (4)$$

The decisive difference is that this changed formulation gives more weight to the KL loss at lower hierarchy levels, leading to more strongly enforcing the unit variance Gaussians nature the KL loss enforces, and therefore hindering noise

from being as easily represented during training. We refer to this architecture as *Altered μ Split* and show qualitative and quantitative results in Section 5 and Tables 1.

The next section extends on *Altered μ Split* by adding unsupervised denoising, adding the last ingredient to the denoiSplit approach we present in this work.

4.3 Adding Suitable Pixel Noise Models

As briefly introduced in Section 2, pixel noise models are a collection of probability distributions mapping from a true pixel intensity to observed noisy pixel measurements (and vice-versa) [16]. They have previously been successfully used in the context of unsupervised denoising [20, 21] and we intend to employ them for this purpose also in the setup we are presenting here. We use the fact that, given a measured (noisy) pixel intensity, a pixel noise model returns a distribution over clean signal intensities and their respective probability of being the underlying true pixel value.

We incorporate this likelihood function into the loss of our overall setup, encouraging denoiSplit to predict pixel intensities that maximize this likelihood and thereby values that are consistent with the noise properties of the given training data.

Since denoiSplit, in contrast to existing denoising applications, predicts two images (the two unmixed channels), we employ two noise models and add two likelihood terms to our overall loss.

More formally, in VAEs [13] and HVAEs, the generative distribution over pixel intensities is modelled as a Gaussian distribution with its variance either clamped to 1 or also learned and predicted. We change our VSE Network to only predict the true pixel intensity and replace the above mentioned Gaussian distribution by distributions defined in two noise models $P_1^{\text{nm}}(c_1^N|c_1)$ and $P_2^{\text{nm}}(c_2^N|c_2)$, one for each respective unmixed output channel. These noise models are pixel-wise independent, *i.e.*,

$$P_i^{\text{nm}}(c_i^N|c_i) = \prod_k P_i^{\text{nm}}(c_i^N[k]|c_i[k]), \quad i \in \{1, 2\}, \quad (5)$$

where $c_i^N[k]$ is the noisy pixel intensity for the k -th pixel and $c_i[k]$ the corresponding noise-free intensity value. This independence makes them particularly suitable for microscopy data where Poisson and Gaussian noise are the predominant pixel-noises one desires to remove.

Since we now directly predict the noise-free pixel values, the output of the decoder can directly be interpreted as $\text{Dec}_\theta(z) = (c_1, c_2)$ and the total loss for denoiSplit now becomes

$$E_{q(z|x;\phi)}[\log P^{\text{nm}}(c_1^N|c_1) + \log P^{\text{nm}}(c_2^N|c_2)] - KL(q(z|x;\phi), P(z)). \quad (6)$$

In [21], two ways for creation of noise models are described and the decision to pick which method depends upon whether or not one has access to the microscope from which data was acquired. In the supplementary Sec S4, we describe

the process of noise model generation and do a quantitative comparison between these two methodologies.

4.4 Computing Calibrated Data Uncertainties

The idea of calibration is for those network setups which produce both prediction and a measure of uncertainty for the prediction.

Networks that can co-assess the uncertainty of their predictions are called calibrated, when the predicted uncertainties are in-line with the measured prediction error. To improve the calibration of a given system, one can find a suitable transformation from uncertainty predictions to measured errors (*e.g.*, the RMSE). After such a transformation is found, an ideal calibrated plot would be tightly fitting $y = x$, with y and x being the error and estimated uncertainty, respectively. See for example Figure 3. Since VSE networks, similar to VAEs, are variational inference systems, we can sample the latent encoding and thereby sample from an approximate posterior distribution of possible solutions given the data uncertainty (aleatoric uncertainty). In this section, our intention is to utilize this ability to predict a reliable uncertainty term for our results.

For this, we adapt the calibration methodology of [18]. In contrast to the approach described there, we propose to use the variability in posterior samples to estimate a pixel-wise standard deviation. More specifically, we sample $k = 50$ predictions for each input image and compute the pixel-wise standard deviations σ_1 and σ_2 for the two predicted image channels \hat{c}_1 and \hat{c}_2 , respectively. This gives us uncertainty predictions.

Next, we calibrate these uncertainty predictions by scaling them appropriately with the help of two learnable scalars, α_1 and α_2 . Following [18], we assume that pixel intensities come from a Gaussian distribution. The mean and the standard deviation of this distribution are the pixel intensities of MMSE prediction, *i.e.* the image obtained after averaging $k = 50$ predictions, and the scaled σ , respectively. We learn the scalars α_1 and α_2 by minimizing the negative log likelihood over the re-calibration dataset. It is important to note that the presented calibration procedure does not alter the original predictions, but instead learns a mapping that best predicts the measured error.

To evaluate the quality of the resulting calibration, we sort the scaled standard deviations $\sigma_i \cdot s_i$ for each pixel in a predicted channel, and build a histogram over $l = 30$ equally sized bins B_i^j . We then compute the root mean variance (RMV) for each bin j and channel i as

$$\text{RMV}_i(j) = \sqrt{\frac{1}{|B_i^j|} \sum_{k \in B_i^j} (\sigma_i^k \cdot \alpha_i)^2}. \quad (7)$$

For each bin B_j and each channel i , we compute the RMSE as

$$\text{RMSE}_i(j) = \sqrt{\frac{1}{|B_i^j|} \sum_{k \in B_i^j} (c_i[k] - \hat{c}_i[k])^2}. \quad (8)$$

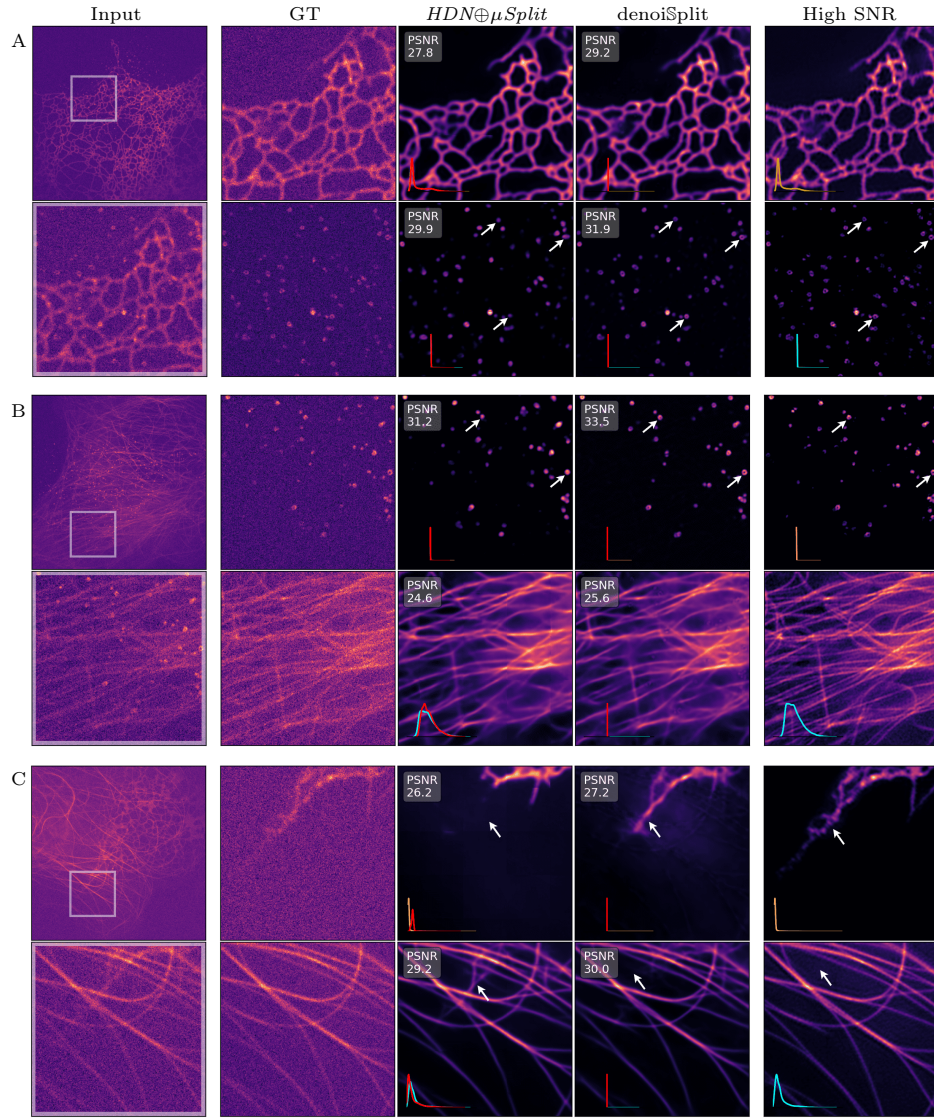


Fig. 4: Comparison to Sequential Baseline. For each panel (ER vs. CCPs, CCPs vs. MT, and ER vs. MT) we show the full mixed input image, a (256×256) inset, corresponding noisy training data crops, the results of the sequential denoising and splitting baseline ($HDN \oplus \mu Split$) and our end-to-end results obtained with denoiSplit. All predictions show the MMSE, obtained by averaging 50 sampled predictions. White arrows indicate locations where the baseline under-performs. Note that such small locations might contribute little to evaluations via PSNR, but makes a huge difference for the downstream analysis of investigated biological structures contained in such microscopy data.

As in Section 3, $c_i[t]$ and $\hat{c}_i[t]$ denote the noise free pixel intensity and the corresponding prediction for i -th channel. In Sec. 5, we plot the RMSE vs. RMV for multiple tasks, observing that the plots closely resemble the identity $y = x$. Following [18], we don't use the training dataset for re-calibration. We use the validation dataset for re-calibration and we show the calibration plots on test dataset.

In supplementary Sec S6, we inspect the relevance of using sampling for estimating unconstrained uncertainty.

5 Experiments and Results

5.1 The BioSR dataset

The BioSR dataset [11] is a comprehensive dataset comprising of fluorescence microscopy images of multiple labeled cell structures. For the purpose of our experiments, we have picked four structures, namely clathrin-coated pits (CCPs), microtubules (MTs), endoplasmic reticulum (ER) and F-actin.

Since the raw data quality is very high and only little image noise is present in the individual micrographs, we add Gaussian noise and Poisson noise of various levels to this raw data. The artificially noisy images are used to train denoiSplit, while the raw data is shown to convince the reader of the validity of our approach and to compute evaluation metrics (see Figs. 2 and 4 and Tab. 1).

In supplementary Sec S1, we evaluate our model on 5 more tasks and these tasks have been created from BioSR, Hagen et al. [10] and PaviaATN [1].

5.2 Synthetic Noise Levels

We work with 4 levels of zero-mean Gaussian noise and two levels of Poisson noise. For Gaussian noise, we compute the standard deviation of the input data X^N for each of the tasks and scale the noise relative to one standard deviation. Specifically, the 4 scaling factors are $\{1, 1.5, 2, 4\}$.

In cases where Poisson noise is added, and since it is already signal dependent, we use a constant factor of 1000 to hit a realistic looking level of Poisson noise. We also consider the case where Poisson noise is not added which we denote by Poisson level of 0 in Tab. 1.

To remove any remaining room for misinterpretations, we provide pseudo-code for the synthetic noising procedure in the supplementary Sec S2.

5.3 Baselines

We conducted all experiments with two baseline setups, μ Split and $HDN \oplus \mu$ Split. In the original μ Split work [1], authors introduce three architectures, but only one of them employs variational inference and is therefore the most suitable to compare against. More specifically, we choose the HVAE + *Regular-LC* setup as described in their work. Here, we simply refer to this baseline as μ Split. Note

that the μ Split baseline makes use of a KL-loss and is therefore enabled to at least partially remove noise from a given noisy input image.

The second baseline, to which we refer to as $HDN\oplus\mu Split$, is a sequential application of Hierarchical DivNoising (HDN), one of the leading unsupervised denoising methods for microscopy datasets [20], and the μ Split setup from above. Hence, here we first denoise all input images x_i^N and the respective two channel images $c_{1,j}^N, c_{2,j}^N$. Note that each set of the three kinds of image are denoised with a separately and specifically trained HDN.

Next, we use the denoised predictions of X^N, C_1^N, C_2^N to train a μ Split network as we did for the first baseline. The expectation from this baseline is to give denoised splitting results which we also show in Fig. 4. We also show the denoised HDN predictions in the supplementary Sec S7.

5.4 Qualitative and Quantitative Evaluation of Results

We show the quality of results our methods can obtain in Figs. 2 to 4.

In Fig. 2, we show predictions on entire input images (960×960 pixels). We can see that μ Split indeed unmixes the given inputs and even partially reduces noise. Still, the results by denoiSplit have a much higher resemblance to the high SNR microscopy images shown in the rightmost column, even though they have never been presented during training (which was conducted only on noisy images as shown in the second column).

In Fig. 3, we show zoomed 256×256 portions of full predictions to allow readers to also appreciate the prediction quality of smaller structures contained in the data. Additionally, we show two posterior samples (S_1 and S_2) as well as their highlighted differences ($S_1 - S_2$). The second to last column shows the average of 50 posterior samples (the approximate MMSE [21]).

In Fig. 4, we also show 256×256 insets on inputs and results by $HDN\oplus\mu Split$ and denoiSplit, showing that fine details are better preserved by our proposed method. Note that it is these very details that make all the difference when such methods are used on fluorescence microscopy data for the sake of scientific downstream analysis.

For quantitative quality evaluations, we use the well known and established PSNR and Multiscale-SSIM metrics [23] to evaluate all results of our experiments and report these results in Tab. 1.

These quantitative evaluations clearly show that our proposed methods improve considerably over μ Split, and as well over the sequential denoising and splitting baseline $HDN\oplus\mu Split$. However, since joint denoising-splitting is an ill-posed problem, it is not difficult to create arbitrarily hard splitting tasks: one just needs to have the two constituent channels contain less discriminatory information. In supplementary Sec S8, we work with a more challenging task to show the limitations of our approach.

Task	Model	training [h]	Noise level parameters							
			$\lambda = 0$				$\lambda = 1000$			
			$\sigma = 1$	1.5	2	4	$\sigma = 1$	1.5	2	4
T1	μ Split	7	30.3 0.853	28.4 0.748	27.4 0.66	25.9 0.42	29.4 0.844	28.1 0.750	27.3 0.667	25.9 0.437
	$HDN \oplus \mu$ Split	11	37.3 0.982	34.9 0.969	33.8 0.959	29.4 0.872	36.3 0.978	34.3 0.965	33.3 0.954	29.4 0.874
	<i>Altered μSplit (ours)</i>	1.3	38.9 0.988	36.7 0.980	34.4 0.965	30.9 0.909	36.9 0.982	35.5 0.974	34.8 0.968	31.1 0.912
	denoiSplit (<i>ours</i>)	1.5	39.7 0.989	36.8 0.978	35.4 0.969	31.1 0.912	37.9 0.984	36.3 0.977	35.0 0.967	31.2 0.912
T2	μ Split	6.3	26.0 0.800	23.9 0.699	22.7 0.593	21.0 0.356	25.2 0.780	23.7 0.691	22.7 0.613	21.1 0.386
	$HDN \oplus \mu$ Split	10	30.1 0.909	28.4 0.873	27.6 0.845	25.3 0.731	29.6 0.904	28.4 0.874	27.4 0.835	25.2 0.738
	<i>Altered μSplit (ours)</i>	1.5	30.4 0.915	28.8 0.879	26.9 0.809	23.4 0.620	29.9 0.903	27.4 0.833	27.9 0.845	24.4 0.677
	denoiSplit (<i>ours</i>)	1.6	30.5 0.916	29.2 0.886	28.2 0.860	25.1 0.714	30.0 0.909	29.0 0.885	27.0 0.815	24.8 0.702
T3	μ Split	7.2	30.5 0.880	28.3 0.793	27.3 0.713	25.6 0.46	29.6 0.877	28.1 0.800	27.2 0.722	25.6 0.476
	$HDN \oplus \mu$ Split	11	38.4 0.981	35.9 0.966	34.3 0.951	29.3 0.844	36.8 0.975	34.9 0.962	33.8 0.948	29.3 0.843
	<i>Altered μSplit (ours)</i>	1.4	38.9 0.985	35.8 0.968	35.0 0.960	30.4 0.867	37.4 0.979	35.6 0.968	34.3 0.953	30.4 0.865
	denoiSplit (<i>ours</i>)	1.6	40.1 0.986	37.3 0.973	35.7 0.962	30.6 0.872	38.1 0.981	36.6 0.971	35.2 0.958	30.7 0.872
T4	μ Split	7	25.9 0.777	24.3 0.664	23.6 0.556	22.4 0.331	25.2 0.729	24.2 0.640	23.5 0.554	22.4 0.321
	$HDN \oplus \mu$ Split	10.7	28.8 0.852	27.9 0.817	27.4 0.790	25.8 0.725	28.2 0.840	27.6 0.810	27.2 0.787	25.7 0.716
	<i>Altered μSplit (ours)</i>	1.3	29.4 0.858	28.5 0.824	27.5 0.786	25.9 0.718	29.0 0.849	27.8 0.794	27.3 0.780	25.8 0.710
	denoiSplit (<i>ours</i>)	1.5	29.6 0.868	28.7 0.835	27.6 0.787	26.0 0.725	29.0 0.854	28.5 0.828	27.9 0.799	26.1 0.727

Table 1: Quantitative Results. We show quantitative evaluations for all joint denoising and splitting experiments. The four corresponding tasks are abbreviated as T1: ER vs. CCPs; T2: ER vs. MT; T3: CCPs vs. MT, T4: F-actin vs. ER. For all experiments, we show the PSNR (sub-row 1) and MS-SSIM (sub-row 2) metrics across 8 noise levels: Gaussian noise levels of $\sigma \in \{1, 1.5, 2, 4\}$ and Poisson noise levels of $\lambda \in \{0, 1000\}$. The best performance per task and noise level is shown in bold. The third column additionally shows the training time on a single Tesla-V100 GPU (in hours). Not only does denoiSplit perform best, it does at the same time require considerably less training time.

6 Discussion and Conclusion

Our work presents denoiSplit, the first method that takes on the challenge of joint semantic image splitting and unsupervised denoising. This advancement is crucial, considering the limitations microscopists face in acquiring high-SNR images, often due to practical constraints such as sample sensitivity and limitations in imaging technology. Unlike in a sequential approach of image denoising followed by training and applying μ Split on denoised data, denoiSplit streamlines the process into a single end-to-end model, which is on one hand reducing the complexity and computational resources required for training and inference, on the other hand leads to better results.

Supporting this conclusion, we presented qualitative and quantitative results, showing that denoiSplit outperforms μ Split, the current SOTA for semantic image splitting, when the available training data is subject to pixel-noises. Since pixel-noises are ubiquitous in biomedical light microscopy, our method addresses an important shortcoming, enabling many potential microscopy users to benefit from the method we devised. Additionally, we have shown that denoiSplit better preserves high-frequency structures of biological samples than the above mentioned sequential pipeline (*i.e.* SOTA denoising followed by μ Split). This is much desired for the downstream analysis of cellular and tissue features in biomedical applications.

Additionally, by leveraging the possibility of performing variational sampling, denoiSplit offers microscopists the opportunity to explore the learned posterior of possible solutions to the joint task at hand. We also present a way to use this sampling capability of denoiSplit to predict the expected error denoiSplit makes on a given input. To this end, we have shown how to calibrate the diversity of samples to best align with the empirically measured error, an approach that can be applied whenever some amount of relatively noise-free calibration data is available. We believe that this is a key contribution of this work, because it enables automated assessment of the data uncertainty in processed images, allowing biologist users without a deep appreciation of the technical details of denoiSplit to remove images from their dataset that should likely not be trusted and therefore not be used for downstream analysis in the context of biomedical investigations.

In the future, we want to explore improved backbone architectures that can further improve the quality of predictions and achievable calibrations. Additionally, domain adaptation techniques to fine-tune existing models on noisy data from slightly different image domains or microscopy modalities would promise to further ease the applicability of denoiSplit by biomedical researchers. This continuous development aims to bridge the gap between computational imaging methods and the practicalities and limitations of modern microscopy, benefiting our overall goal of elevating the rate of scientific discovery in the life-sciences by conducting cutting-edge methods research.

References

1. Ashesh, Krull, A., Sante, M.D., Pasqualini, F.S., Jug, F.: μ Split: image decomposition for fluorescence microscopy (2023) [1](#), [2](#), [4](#), [5](#), [6](#), [11](#), [S.2](#), [S.6](#), [S.7](#), [S.8](#)
2. Bahat, Y., Irani, M.: Blind dehazing using internal patch recurrence. In: 2016 IEEE International Conference on Computational Photography (ICCP). pp. 1–9 (May 2016) [4](#)
3. Batson, J., Royer, L.: Noise2Self: Blind denoising by Self-Supervision pp. 1–16 (Jan 2019) [2](#)
4. Berman, D., Treibitz, T., Avidan, S.: Non-local image dehazing. In: 2016 IEEE Conference on Computer Vision and Pattern Recognition (CVPR). pp. 1674–1682. IEEE (Jun 2016) [4](#)
5. Buades, A., Coll, B., Morel, J.M.: A non-local algorithm for image denoising. 2005 IEEE computer society (2005) [2](#)
6. Dabov, K., Foi, A., Katkovnik, V., Egiazarian, K.: Image denoising by sparse 3-D transform-domain collaborative filtering. IEEE Trans. Image Process. **16**(8), 2080–2095 (Aug 2007) [2](#)
7. Dekel, T., Rubinstein, M., Liu, C., Freeman, W.T.: On the effectiveness of visible watermarks (2017) [4](#)
8. Gandelsman, Y., Shocher, A., Irani, M.: “Double-DIP” : Unsupervised image decomposition via coupled deep-image-priors (2019), accessed: 2022-2-14 [4](#)
9. Ghiran, I.C.: Introduction to fluorescence microscopy. Methods Mol. Biol. **689**, 93–136 (2011) [1](#)
10. Hagen, G.M., Bendesky, J., Machado, R., Nguyen, T.A., Kumar, T., Ventura, J.: Fluorescence microscopy datasets for training deep neural networks. Gigascience **10**(5) (May 2021) [11](#), [S.2](#)
11. Jin, L., Liu, J., Zhang, H., Zhu, Y., Yang, H., Wang, J., Zhang, L., Xu, Y., Kuang, C., Liu, X.: Deep learning permits imaging of multiple structures with the same fluorophores. bioRxiv (2023) [11](#)
12. Kingma, D.P., Salimans, T., Welling, M.: Improving variational inference with inverse autoregressive flow. CoRR [abs/1606.04934](#) (2016), <http://arxiv.org/abs/1606.04934> [S.2](#)
13. Kingma, D.P., Welling, M.: An introduction to variational autoencoders (Jun 2019) [8](#)
14. Ko, J., Lee, S.: Self2Self+: Single-Image denoising with Self-Supervised learning and image quality assessment loss (Jul 2023) [2](#)
15. Krull, A., Buchholz, T.O., Jug, F.: Noise2Void - learning denoising from single noisy images. arXiv [cs.CV](#), 2129–2137 (Nov 2018) [2](#), [S.4](#)
16. Krull, A., Vicar, T., Prakash, M., Lalit, M., Jug, F.: Probabilistic Noise2Void: Unsupervised Content-Aware denoising. Frontiers in Computer Science **2**, 60 (Feb 2020) [2](#), [4](#), [8](#)
17. Lehtinen, J., Munkberg, J., Hasselgren, J., Laine, S., Karras, T., Aittala, M., Aila, T.: Noise2Noise: Learning image restoration without clean data. arxiv.org (Mar 2018) [4](#)
18. Levi, D., Gispan, L., Giladi, N., Fetaya, E.: Evaluating and calibrating uncertainty prediction in regression tasks. Sensors **22**(15) (2022) [4](#), [9](#), [11](#)
19. Platt, J.: Probabilistic outputs for support vector machines and comparisons to regularized likelihood methods. Adv. Large Margin Classif. **10** (06 2000) [4](#)
20. Prakash, M., Delbracio, M., Milanfar, P., Jug, F.: Interpretable unsupervised diversity denoising and artefact removal (Apr 2021) [2](#), [4](#), [5](#), [6](#), [8](#), [12](#)

21. Prakash, M., Krull, A., Jug, F.: DivNoising: Diversity denoising with fully convolutional variational autoencoders. ICLR 2020 (Jun 2020) [2](#), [4](#), [8](#), [12](#), [S.3](#), [S.4](#)
22. Prakash, M., Lalit, M., Tomancak, P., Krull, A., Jug, F.: Fully unsupervised probabilistic Noise2Void. arXiv [eess.IV](#) (Nov 2019) [2](#), [4](#)
23. Shroff, H., Testa, I., Jug, F., Manley, S.: Live-cell imaging powered by computation. Nat. Rev. Mol. Cell Biol. (Feb 2024) [1](#), [2](#), [12](#)
24. Sønderby, C.K., Raiko, T., Maaløe, L., Sønderby, S.K., Winther, O.: Ladder variational autoencoders. Adv. Neural Inf. Process. Syst. **29**, 3738–3746 (Jan 2016) [5](#)
25. Ulyanov, D., Vedaldi, A., Lempitsky, V.: Deep image prior. Int. J. Comput. Vis. **128**(7), 1867–1888 (Jul 2020) [2](#)
26. Weigert, M., Royer, L., Jug, F., Myers, G.: Isotropic reconstruction of 3D fluorescence microscopy images using convolutional neural networks. In: Medical Image Computing and Computer-Assisted Intervention - MICCAI 2017. pp. 126–134. Springer International Publishing (2017) [2](#)
27. Weigert, M., Schmidt, U., Boothe, T., Müller, A., Dibrov, A., Jain, A., Wilhelm, B., Schmidt, D., Broaddus, C., Culley, S., Rocha-Martins, M., Segovia-Miranda, F., Norden, C., Henriques, R., Zerial, M., Solimena, M., Rink, J., Tomancak, P., Royer, L., Jug, F., Myers, E.W.: Content-aware image restoration: pushing the limits of fluorescence microscopy. Nature Publishing Group **15**(12), 1090–1097 (Dec 2018) [2](#), [4](#), [S.2](#)
28. Zhang, K., Zuo, W., Chen, Y., Meng, D., Zhang, L.: Beyond a gaussian denoiser: Residual learning of deep CNN for image denoising. IEEE Trans. Image Process. **26**(7), 3142–3155 (Jul 2017) [2](#)

Supplementary Material denoiSplit: a method for joint image splitting and unsupervised denoising

Ashesh, Florian Jug
Jug Group, Fondazione Human Technopole, Milano, Italy,

Task	Model	training [h]	Noise level parameters							
			$\lambda = 0$				$\lambda = 1000$			
			$\sigma = 1$	1.5	2	4	$\sigma = 1$	1.5	2	4
T5	μ Split	5.5	25.1	23.7	23.1	22.1	24.8	23.8	23.0	22.1
			0.728	0.633	0.537	0.341	0.697	0.593	0.536	0.307
	$HDN \oplus \mu$ Split	8	27.3	26.6	26.1	24.6	27.4	26.4	26.1	24.3
			0.793	0.756	0.731	0.645	0.794	0.739	0.722	0.639
	<i>Altered μSplit (ours)</i>	1.3	27.9	26.8	25.9	24.5	27.4	26.5	25.9	24.4
			0.799	0.741	0.698	0.601	0.780	0.731	0.697	0.595
	denoiSplit (<i>ours</i>)	1.5	27.7	27.0	25.9	24.5	27.5	27.1	26.0	24.4
			0.798	0.762	0.707	0.604	0.787	0.761	0.710	0.606
T6	μ Split	5	30.5	28.7	27.8	26.7	29.9	28.7	27.9	26.8
			0.869	0.779	0.685	0.422	0.866	0.788	0.708	0.443
	$HDN \oplus \mu$ Split	7	34.6	33.1	32.1	28.8	33.8	32.6	32.0	28.8
			0.938	0.907	0.885	0.785	0.926	0.899	0.882	0.783
	<i>Altered μSplit (ours)</i>	1.3	35.5	33.3	32.5	30.4	34.4	32.8	32.4	30.1
			0.950	0.911	0.890	0.825	0.935	0.898	0.887	0.819
	denoiSplit (<i>ours</i>)	1.5	36.3	34.4	33.1	30.4	34.7	33.8	32.9	29.9
			0.945	0.927	0.895	0.830	0.939	0.918	0.890	0.826

Table S.1: Quantitative Results. We show quantitative evaluations for two more tasks which are abbreviated as T5: F-actin vs. MT and T6: F-actin vs CCPs. For all experiments, we show the PSNR (sub-row 1) and MS-SSIM (sub-row 2) metrics across 8 noise levels: Gaussian noise levels of $\sigma \in \{1, 1.5, 2, 4\}$ and Poisson noise levels of $\lambda \in \{0, 1000\}$. The best performance per task and noise level is shown in bold. The third column additionally shows the training time on a single Tesla-V100 GPU (in hours).

S.1 Performance on more splitting tasks

In this section, we train our models and baselines on **five more tasks**. We train two tasks from BioSR dataset. Specifically, we add F-actin *vs.* CCPs and F-actin *vs.* Microtubules tasks. In Tab. S.1, we present the quantitative evaluation on these two tasks. Similar to the results from the Table 1 of main manuscript, here as well, we find our methods, specifically denoiSplit to outperform others in most cases.

We worked on three additional joint denoising-splitting tasks from two other datasets which we describe next.

Hagen et al. Actin-Mitochondria Dataset We picked the high resolution Actin and Mitochondria channels from Hagen et al. [10] which were also used in [1]. Additionally, we also worked with the low SNR version of these channels provided in the dataset as yet another task. Note that in this task, the channels had the real microscopy noise present in them.

PaviaATN dataset [1] We worked with the Actin and Tubulin channel provided by the dataset. It is worth noting that in terms of PSNR, we picked the hardest of the three tasks worked upon by Ashesh et al. [1].

We provide the results on tasks generated from PaviaATN and Hagen et al. datasets in Tab. S.2. We discuss more on these results in Sec. S.8. We show the full-frame predictions for tasks not shown in the main manuscript in Figs. S.4 to S.7.

S.2 Hyperparameter and Training details

As stated in the main manuscript, our denoiSplit and *Altered μ Split* are built on top of μ Split architecture. In addition to the major changes which are discussed in the main manuscript, we have enabled *free bits* [12] parameter and have set *free bits* = 1. We also do not use any additional low-resolution inputs.

denoiSplit, *Altered μ Split* and HDN have been trained with the learning rate of 0.001, batch size of 32, patch size of 128, max epoch of 400 and with 16 bit precision. For every task, 80% of the data was allocated as training data, 10% of the data as validation data and 10% as the test data. For μ Split baseline and used as part of *HDN \oplus μ Split*, we use the same training configuration as mentioned in [1]. For PSNR, we use the range invariant PSNR formulation which is commonly used in this field [1, 27].

We have provided code with this supplement where information about how Poisson noise is added is present in the file *vanilla_dloader.py:L175*. Specifically, we use numpy python package to add poisson noise as

$$\text{data} = \text{np.random.poisson}(\text{data}/\text{poisson_factor}) * \text{poisson_factor} \quad (1)$$

We use *poisson_factor* = 1000. Finally, in Tab. S.3, we provide the actual σ values which were used to add Gaussian noise in different tasks.

S.3 Practical relevance of denoiSplit

Here, we outline the intended usecase for our work. Similar to [1], our work also aims to enable microscopists in extracting multiple structures using a single fluorescence marker. There are two important practical considerations which our work addresses.

Firstly, different microscopy projects, depending upon the nature of underlying specimen and microscope type, have different tolerance for the amount of laser power and the dwell time which can be used during acquisition. This roughly translates to the amount of noise which will be present in the acquired micrographs. In this work, we cater to this necessity by working with different noise levels.

Secondly, in most cases, there will be a need to purchase a single fluorescent marker which can bind to both cellular structure types one is interested in. Additionally, even after the purchase, it might still be challenging to get a decent staining of both structures with the marker. An imperfect staining can lead to under-expression of one of the two structure types in the imaged micrographs. Therefore, there is also an investment of time and expertise in getting a proper staining. That being the case, it makes sense to first inspect the feasibility of the approach before making the investment of buying a new marker followed by getting the staining correct. Our method provides the way to get proof-of-concept splitting without making any of these investments.

We envision that microscopists should image individual channels in the same noise regime as is permitted in their project. They should then train the denoiSplit and inspect the prediction quality. If there is a room for adjustment in power and dwell time, they can re-acquire in a different noise regime and train the denoiSplit again. Note that this acquisition can be done with a single-color setup and therefore can be done using their existing microscope configuration.

In case they find the model performance satisfactory in some feasible noise regime, they can then order the relevant fluorescent marker and can subsequently label their structures with it to get superimposed images. Finally, they need to finetune the trained network to this slightly different input data and then they can start using denoiSplit. This problem of finetuning the model is outside the scope of this work and will be taken up in our future work.

denoiSplit also enables sampling which, as stated in the main manuscript, will enable microscopists to inspect the predictions to get a visual feeling about uncertain areas in prediction. To showcase this, we provide with this supplement, a *sampling.gif* file where one could see 50 samples on a randomly chosen input from MT *vs.* ER task.

S.4 Noise model generation

Depending upon the physical availability of microscope, [21] described two ways in which the noise model can be generated. In this section, our motivation is to assess the performance difference which one should expect between these two ways. We find that different choices of noise model generation do not lead to very different performances. This result enables denoiSplit to be used across a wide variety of scenarios.

S.4.1 Physical availability of Microscope

The simpler and the better case is when we have access to the microscope which generated the noisy data. In this case, one needs to image the same content N times which would result in acquisition of N noisy versions of the same underlying specimen. The high SNR version is then computed by simply taking the pixelwise average of these noisy samples. In this situation, for every clean signal value, one has N noisy intensities. This data is then used to train the Gaussian mixture based noise model.

To simulate this condition, for every intensity value in the range $[0, 65535]$, we obtain multiple noisy intensity values by adding the noise (Gaussian and/or Poisson) multiple times independently.

S.4.2 Physical unavailability of Microscope

In case the microscope is not available, which is true for all publicly available microscopy datasets, [21] proposed a bootstrap noise model approach. In this method, the idea was to denoise the noisy data using some unsupervised/self-supervised denoising technique and use the noisy data and the predicted denoised data to generate the noise model.

To simulate this condition, we added noise to the noise free training data. This gave us the noisy data and clean data pair which we used to train the noise model. To showcase the applicability of our method to all publicly available datasets, we have generated all noise models using this approach.

It is worth noting that in the way described above, there is a source of error which has not been captured. This is the error introduced by the denoising process for getting the clean data from its noisy counterpart. To assess the effect of denoising, we generate the noise model in yet another way. In this way, we added the noise to the noise free training data. We then use N2V [15], an off-the-shelf denoiser to denoise the images. We use the noisy data and the denoised images to generate the noise model.

S.4.3 Performance comparison among different noise model generation procedures

To assess how performance varies depending upon the methodology used for noise model creation which have been described above subsections, we train denoiSplit three times, each time with its noise model computed using a different way. In Fig. S.1, we show the performance comparison. denoiSplit+ S_∞ denotes the case when one has access to microscope. denoiSplit+S1 denotes the case when one works with a noisy and its clean data pair. denoiSplit+N2V denotes the case when one obtains the clean data after denoising with N2V. We train them on two tasks namely ER *vs.* CCPs and ER *vs.* MT over four Gaussian noise levels with Poisson noise ($\lambda = 1000$) enabled. As can be observed from the plots, we don't see a large difference between the three approaches.

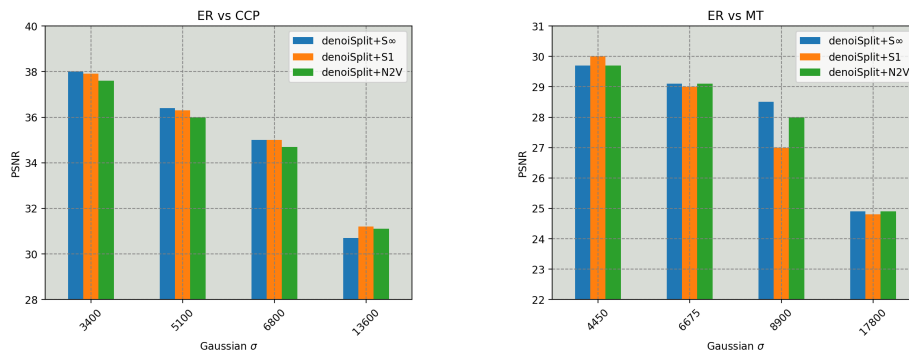


Fig.S.1: Quantitative comparison of different noise model generation methodologies: Here, we compare three ways in which noise models can be generated. (a) denoiSplit+S ∞ : When for every clean pixel intensity, one has access to multiple noisy intensities. This corresponds to the case when one has access to the microscope which has generated the data. (b) denoiSplit+S1: This corresponds the case when one has access to clean data and its corresponding noisy data. (c) denoiSplit+N2V: This corresponds to the case when one has access to just noisy data. We use N2V to denoise them which we use as clean data. We compare denoiSplit trained using each of the three noise model variants. We show PSNR performance on two tasks.

This performance evaluation encourages denoiSplit to be used on publicly available datasets and for proof-of-concept evaluations since it shows that having access to the microscope does not give large performance improvements and the **bottleneck in denoising-splitting is essentially the splitting task.**

S.5 Comparison between denoising task and splitting task

In this section, we compare between two computer vision tasks which are of relevance to us: (a) unsupervised denoising and (b) joint denoising-splitting. From Fig. S.2, we observe that unsupervised denoising is arguably a simpler task when compared to joint denoising-splitting. The PSNR between the prediction and high SNR micrographs is much better for HDN as compared to denoiSplit for most cases. We note that it is expected because in joint denoising-splitting, besides denoising, which is the sole task in unsupervised denoising, one needs to additionally do the job of image decomposition. But more interestingly, we observe that the prediction quality of one channel depends upon the other channel.

We note that this observation is of considerable importance because it opens up the question of best pairing strategy: which two structures should be imaged by a single color fluorescent marker? This will be part of our future work.

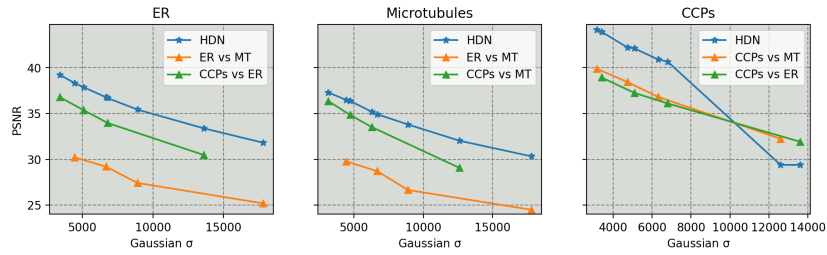


Fig. S.2: Problem comparison: Joint Denoising-Splitting vs. Denoising In this figure, we compare the PSNR with respect to high-SNR micrographs for two image restoration tasks: (a) Self-supervised denoising for which we use HDN and (b) joint denoising-splitting where denoiSplit is used. We evaluate the two models over multiple noise levels of Gaussian noise (x-axis) with Poisson($\lambda = 1000$) noise present in all cases. For denoiSplit, we use three tasks namely: ER vs. MT, CCPs vs. ER and CCPs vs MT. We show one plot for each structure type (ER, Microtubules and CCPs). Two things are evident: (a) Judging just from PSNR numbers, we can say that Denoising is a simpler task than joint Denoising-Splitting. (b) Performance of denoiSplit for one channel depends on the other channel as well. For example, for denoiSplit, PSNR on ER channel (first plot) is higher when the task is CCPs vs. ER (green) as opposed to ER vs. MT (orange) task.

S.6 On usefulness of using sampling for calibration

In this section, we investigate our choice for estimating un-calibrated uncertainty using sampled predictions. For this, we estimate the uncalibrated pixelwise uncertainty using varying number of samples. We then follow our calibration procedure and learn the channelwise scalar to get the calibration plot. As can be observed in Fig. S.3, as we increase the number of samples, the calibrated plot also improves thereby validating our choice.

S.7 Qualitative evaluation of HDN denoising

Here, we qualitatively evaluate the denoising behaviour of HDN. We show three random input patches and the corresponding channel first and channel second crops from 6 different splitting tasks in Figs. S.8 to S.13. We show the results on noisy dataset having Poisson($\lambda = 1000$) noise and Gaussian noise of relative scale 1.5. Since main manuscript also shows the qualitative figures on this noise level, we believe this can be used together with the figures present in main manuscript to better understand the behaviour of $HDN \oplus \mu Split$.

S.8 Failure cases: Avenues for future work

In this section, we inspect the worse performing cases in our work. One clear example is Actin vs. Tubulin task from PaviaATN [1] dataset whose quantitative

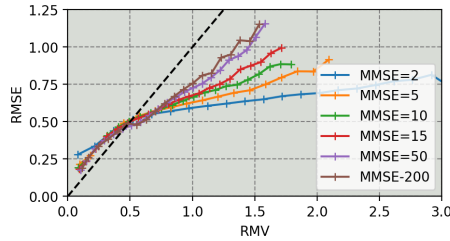


Fig. S.3: In this figure, we show that as we increase the sample count to get the uncalibrated estimate of pixelwise uncertainty, the calibration diagram as shown in this plot becomes better and better, *i.e.*, gets more and more closer to $y = x$.

evaluation is present in Tab. S.2. However, as can be seen from Fig. S.14, we find performance of both $HDN \oplus \mu Split$ and denoiSplit to be unsatisfactory for it to be used by microscopists. We note a striking difference of this task with the tasks from BioSR dataset. Looking at 128×128 input patches for tasks from BioSR data, one could visually form an opinion about which structures in the input patch should belong to first channel and which to the second channel. In case of Actin *vs.* Tubulin task, we observe that making this opinion is much more difficult since local structures are much less discriminative. It is only when looking at a larger context, one can form some opinion about which structures should be present in which channel. There seems to be another factor related to the nature of the structures which the channels are composed of. Informally speaking, individual channels have a "surface" like structure in Actin and Tubulin images of PaviaATN dataset as opposed to "curved lines", "mesh" and "dots" like structures in BioSR dataset.

Between denoiSplit and $HDN \oplus \mu Split$, we observe that for this task, denoiSplit has more tiling artefacts. It is not surprising for that to be the case because in [1], the Lateral contextualization (LC) approach which incorporates context in a memory efficient way, worked well on Actin *vs.* Tubulin. Compared to $HDN \oplus \mu Split$, our model is naturally at disadvantage because we have disabled the LC module but $HDN \oplus \mu Split$ uses it. We believe that increasing the patch size can help our denoiSplit reduce the tiling artefacts.

In general, we also find cases where $\mu Split$ has retained some fine structures, albeit with noise, which the denoising based approaches have omitted from the prediction. We argue this to be a natural consequence of restricting the expressivity of latent spaces with KL divergence loss, which is pivotal for denoising.

As joint denoising-Splitting is a new task, there is much that needs to be done. We humbly acknowledge the challenges mentioned above which we hope to tackle in our future works.

Model	Tasks								
	T7				T8				T9
	1	1.5	2	4	1	1.5	2	4	
μ Split	22.6	21.1	20.2	19.1	28.7	27.0	26.2	25.2	26.5
	0.555	0.442	0.361	0.189	0.905	0.825	0.747	0.489	0.887
$HDN \oplus \mu Split$	27.8	27.3	27.0	26.4	-	-	-	-	28.1
	0.880	0.871	0.865	0.843	-	-	-	-	0.760
(Ours) <i>Altered μSplit</i>	26.3	26.2	25.9	25.2	34.7	34.2	33.6	32.3	31.1
	0.838	0.826	0.820	0.807	0.975	0.971	0.966	0.951	0.887
(Ours) denoisplit	26.4	26.1	26.0	25.2	35.5	33.7	33.5	32.2	31.0
	0.835	0.827	0.825	0.807	0.979	0.974	0.968	0.951	0.887

Table S.2: T7: Actin vs Tubulin from PaviaATN dataset, T8: Actin vs Mito, T9: Actin vs Mito low SNR. For Hagen et al. dataset tasks (T8 and T9), HDN training was quite unstable and crashed multiple times due to NaNs. Due to this reason, there are no entries for $HDN \oplus \mu Split$ for the task T8. For task T9, we were able to train the $HDN \oplus \mu Split$ with a lower hierarchy count (3 as opposed to default 6). For T9, similar to [1], we also upper bounded the log of variance of the latent space to 20 across all hierarchy levels for further stability.

Task	$\sigma = 1$	$\sigma = 1.5$	$\sigma = 2$	$\sigma = 4$
ER vs. CCPs	3400	5100	6800	13600
ER vs. MT	4450	6675	8900	17800
CCPs vs. MT	3150	4725	6300	12600
F-actin vs. ER	4450	6675	8900	17800
F-actin vs. CCPs	3050	4575	6100	12200
F-actin vs. MT	4300	6450	8600	17200

Table S.3: Gaussian σ values for the different tasks. Note that they have been estimated by computing the standard deviation on the input images of these tasks.

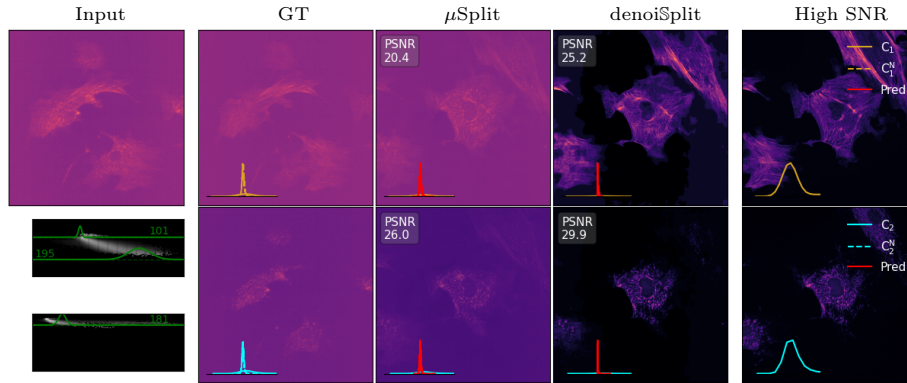


Fig.S.4: Qualitative Results Actin vs. Mito: In this figure, we show full frame prediction on Actin *vs.* Mitochondria task. Here, the noise in the target channels is not synthetic but is real microscopy noise. We show noisy input (column one), individual noisy channel training data (column two), and predictions by one of the baselines μ Split (column three) and our own results obtained with denoiSplit (column four). Additionally we show high SNR channel images (not used during training) as the last column and show PSNR values w.r.t. these images. Additionally, we plot histograms of pixel intensities various panels for comparison (see legend on the right). The second row, first column shows the used noise models. The superimposed plots (green) show the distribution of noisy observations (c_i^N) for two clean signal intensities.

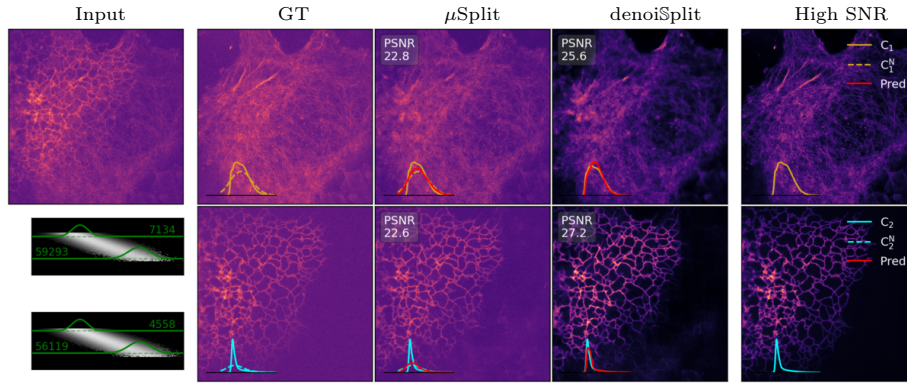


Fig.S.5: Qualitative Results F-actin vs. ER: In this figure, we show full frame prediction on F-actin *vs.* ER task. We show noisy input (column one), individual noisy channel training data (column two), and predictions by one of the baselines μ Split (column three) and our own results obtained with denoiSplit (column four). Additionally we show high SNR channel images (not used during training) as the last column and show PSNR values w.r.t. these images. Additionally, we plot histograms of pixel intensities various panels for comparison (see legend on the right). The second row, first column shows the used noise models. The superimposed plots (green) show the distribution of noisy observations (c_i^N) for two clean signal intensities.

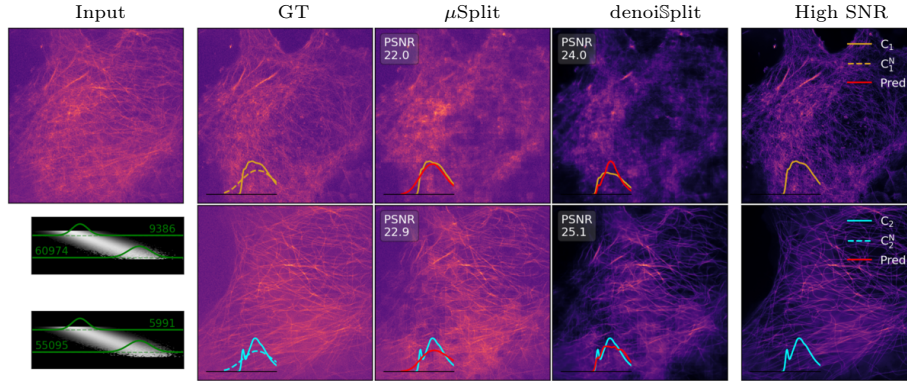


Fig. S.6: Qualitative Results F-actin vs. MT: In this figure, we show full frame prediction on F-actin *vs.* MT task. We show noisy input (column one), individual noisy channel training data (column two), and predictions by one of the baselines μ Split (column three) and our own results obtained with denoiSplit (column four). Additionally we show high SNR channel images (not used during training) as the last column and show PSNR values w.r.t. these images. Additionally, we plot histograms of pixel intensities various panels for comparison (see legend on the right). The second row, first column shows the used noise models. The superimposed plots (green) show the distribution of noisy observations (c_i^N) for two clean signal intensities.

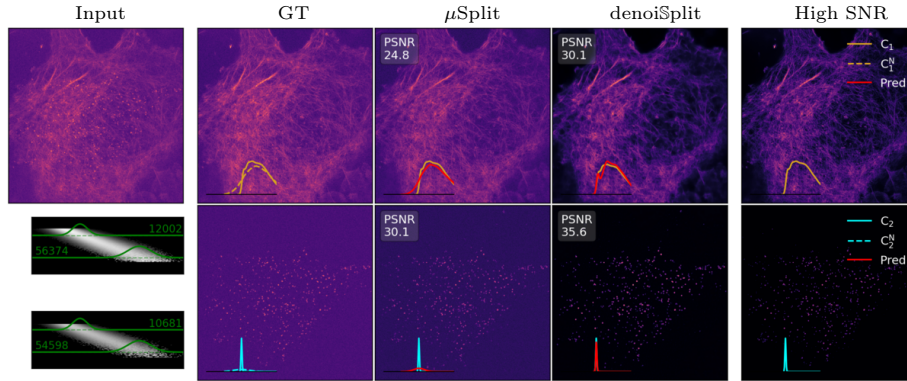


Fig. S.7: Qualitative Results F-actin vs. CCPs: In this figure, we show full frame prediction on F-actin *vs.* CCPs task. We show noisy input (column one), individual noisy channel training data (column two), and predictions by one of the baselines μ Split (column three) and our own results obtained with denoiSplit (column four). Additionally we show high SNR channel images (not used during training) as the last column and show PSNR values w.r.t. these images. Additionally, we plot histograms of pixel intensities various panels for comparison (see legend on the right). The second row, first column shows the used noise models. The superimposed plots (green) show the distribution of noisy observations (c_i^N) for two clean signal intensities.

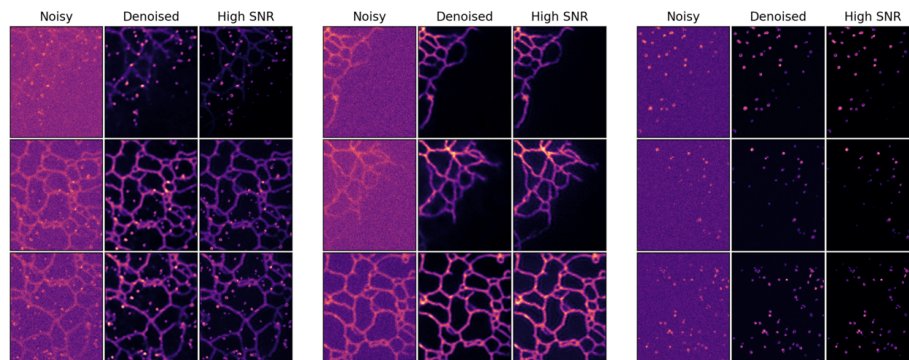


Fig. S.8: Qualitative performance of HDN on ER *vs.* CCPs task input and its two constituent channels. Left panel shows the denoising performance on input for our splitting task and central and right panel shows its denoising performance on its two constituent channels. Within each panel, we show three random patches (rows) of size 256×213 . Specifically, we show the input (first column), denoised predictions (second column) and high SNR patch (last column).

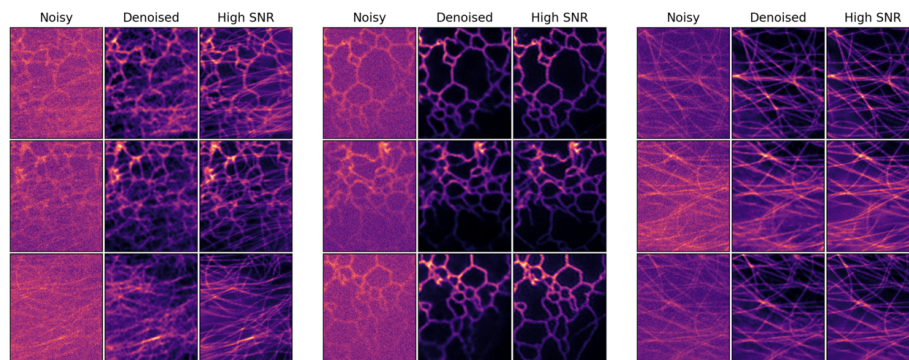


Fig. S.9: Qualitative performance of HDN on ER *vs.* MT task input and its two constituent channels. Left panel shows the denoising performance on input for our splitting task and central and right panel shows its denoising performance on its two constituent channels. Within each panel, we show three random patches (rows) of size 256×213 . Specifically, we show the input (first column), denoised predictions (second column) and high SNR patch (last column).

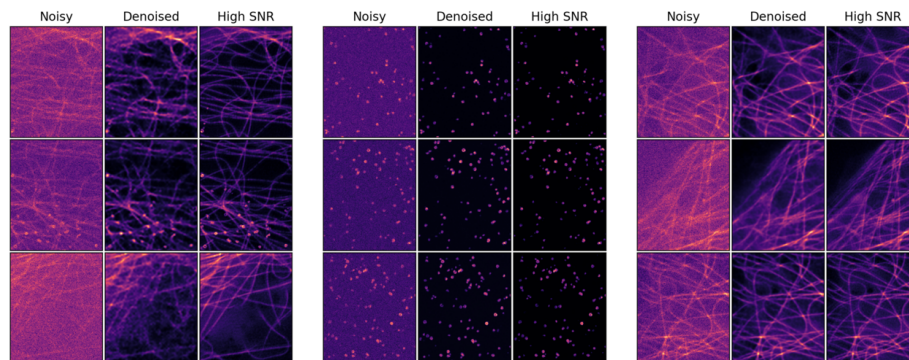


Fig. S.10: Qualitative performance of HDN on CCPs *vs.* MT task input and its two constituent channels. Left panel shows the denoising performance on input for our splitting task and central and right panel shows its denoising performance on its two constituent channels. Within each panel, we show three random patches (rows) of size 256×213 . Specifically, we show the input (first column), denoised predictions (second column) and high SNR patch (last column).

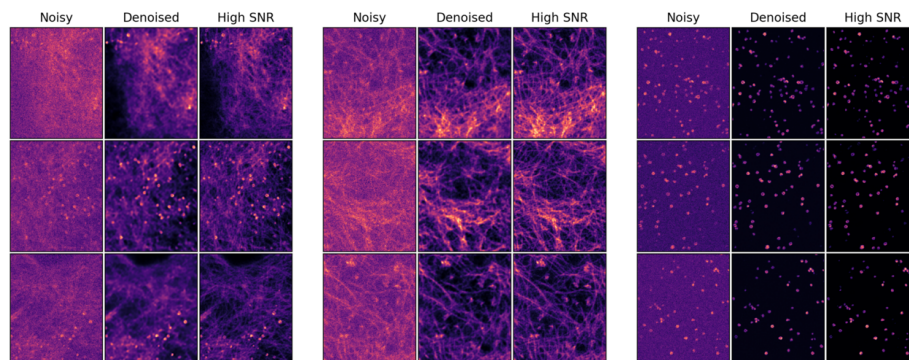


Fig. S.11: Qualitative performance of HDN on F-actin *vs.* CCPs task input and its two constituent channels. Left panel shows the denoising performance on input for our splitting task and central and right panel shows its denoising performance on its two constituent channels. Within each panel, we show three random patches (rows) of size 256×213 . Specifically, we show the input (first column), denoised predictions (second column) and high SNR patch (last column).

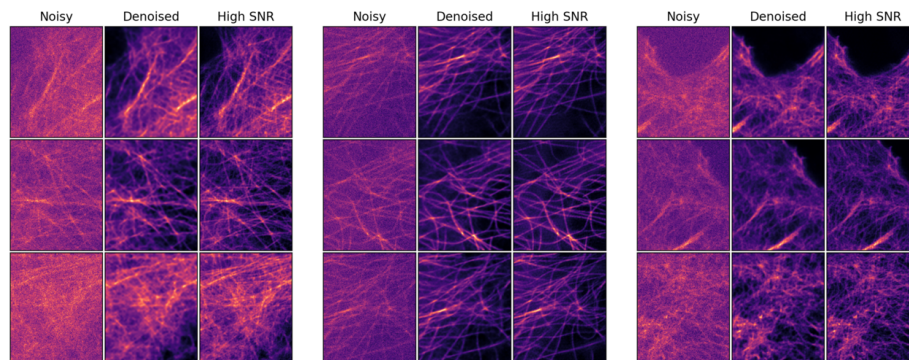


Fig. S.12: Qualitative performance of HDN on F-actin *vs.* MT task input and its two constituent channels. Left panel shows the denoising performance on input for our splitting task and central and right panel shows its denoising performance on its two constituent channels. Within each panel, we show three random patches (rows) of size 256×213 . Specifically, we show the input (first column), denoised predictions (second column) and high SNR patch (last column).

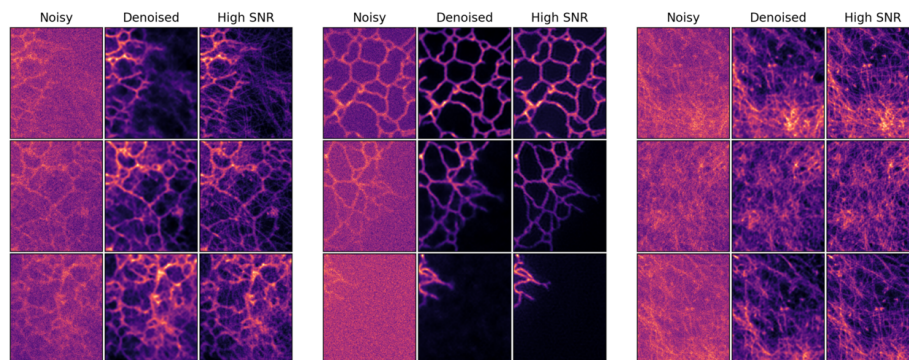


Fig. S.13: Qualitative performance of HDN on F-actin *vs.* ER task input and its two constituent channels. Left panel shows the denoising performance on input for our splitting task and central and right panel shows its denoising performance on its two constituent channels. Within each panel, we show three random patches (rows) of size 256×213 . Specifically, we show the input (first column), denoised predictions (second column) and high SNR patch (last column).

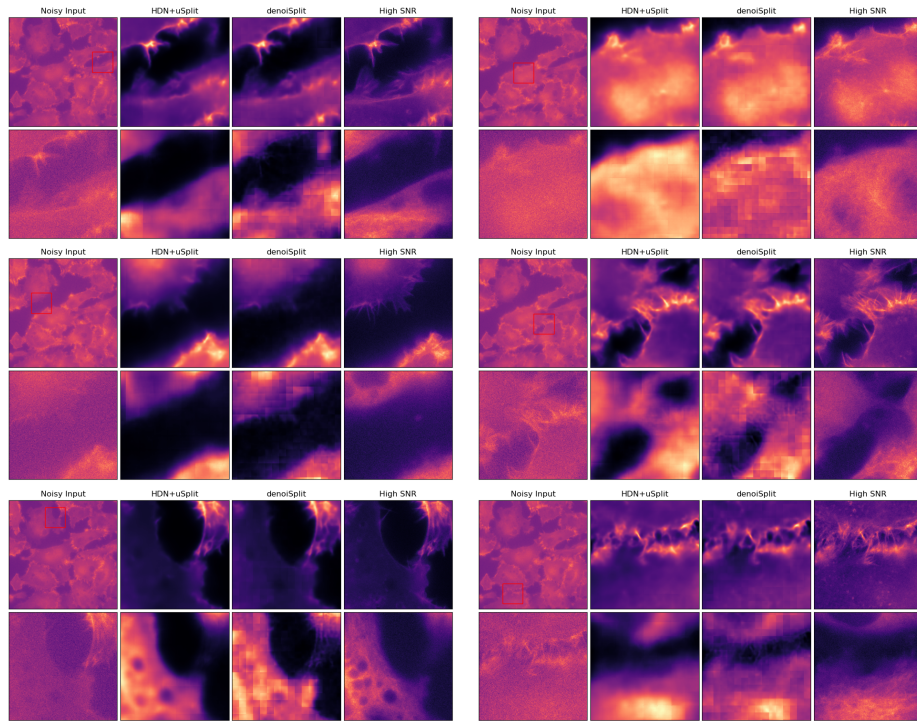


Fig.S.14: PaviaATN Actin vs. Tubulin task Here, we show performance of denoiSplit and $HDN \oplus \mu Split$ for six random input patches of size 500×500 in six panels. Within each panel, we show the full input frame and its crop for which we do the predictions (column one). Next two columns have the predictions of $HDN \oplus \mu Split$ and denoiSplit respectively. The last column is the high SNR ground truth. We observe that the splitting performance of both $HDN \oplus \mu Split$ and denoiSplit does not reach the quality at which microscopists would find it useful. Between $HDN \oplus \mu Split$ and denoiSplit, we see more tiling artefacts for denoiSplit.